

Bachelor thesis

Written by Magnus Quaade Oddershede
Niels Bohr Institute

Modelling of Ocean Turbulence

Effects of resolution on predictive power of ocean models

15-June-2022

Under supervision of Markus Jochum

Institute: Niels Bohr Institute
Department: Physics of Ice, Climate and Earth
Author: Magnus Quaade Oddershede
Supervisor: Markus Jochum
Title and subtitle: Modelling of Ocean Turbulence
Effects of resolution on predictive power of ocean models
Front page image: by Magnus Quaade Oddershede
Handed in: 15-June-2022
Defended: 22-June-2022

Signed by Magnus Quaade Oddershede



Signed on 15-June-2022

Abstract

The oceans play a large role in global climate models by distributing physical quantities like heat around the Earth. It is therefore important that ocean models used in large-scale climate simulations produce accurate and reliable results. Leading global ocean models like the Community Earth System Model feature a horizontal resolution of 1° and use turbulent viscosity parameterization of small-scale turbulence grounded theoretically in Prandtl's mixing length model. In the present work, an idealized ocean has been numerically modeled using a coarse-resolution model and a high-resolution model with horizontal resolutions of 1° and 0.1° , respectively. The coarse-resolution model uses turbulent viscosity parameterization of small-scale turbulence. The results of these simulations have been used to compare the general mean flow characteristics of high- and low-resolution models and to investigate whether the assumptions behind Prandtl's mixing length model are representative for an ocean based on the high-resolution model. The study finds that significant mean-flow structure found in the high-resolution model is absent in the coarse-resolution model and that the width of the western boundary current is underestimated in the coarse-resolution model. This study further finds that Prandtl's mixing length model fails to predict the magnitude and structure of small-scale turbulence based on the turbulent viscosity parameterization via the mean flow.

Table of content

1	Introduction	5
1.1	General purpose and structure	5
1.2	Oceanic length scales and numerical limitations	5
1.3	Reynolds averaging and the turbulence closure problem	6
1.4	The Boussinesq hypothesis and Prandtl’s mixing length model	7
1.5	Sverdrup’s balance	8
1.6	Gyres and western boundary currents	8
1.7	Analyzing discrete ocean model results	9
2	Model setup	11
2.1	Versatile Ocean Simulator (VEROS)	11
2.2	Model domain, forcings, and model setup	11
2.3	Model initiation and data collection	12
3	Results	12
3.1	Model validation	12
3.1.1	Spin-up analysis	12
3.1.2	Checking the general circulation	13
3.2	General characteristics of the gyres	15
3.2.1	Mean, interior flow	15
3.2.2	Western boundary current	15
3.2.3	Turbulence	16
3.3	Characteristic length scales	17
3.4	Characteristic velocity scale	19
3.5	Checking Prandtl’s mixing length model	19
4	Discussion	21
5	Conclusion	23
A	Appendix	25
A.1	25
A.2	25
A.3	25

1 Introduction

1.1 General purpose and structure

The present thesis aims to explore the effects of turbulence on the mean flow of discretized, numerical ocean models with a finite spatial resolution. For this purpose, a numerical model of an idealized, rectangular ocean has been made using the Versatile Ocean Simulation in Pure Python (VEROS). The basin corresponds roughly to the Northern Atlantic Ocean in terms of size and meridional position. Specifically, it will be examined how the results of a high-resolution, turbulence-resolving model (0.1° horizontal resolution) differ from those of a coarse-resolution model (1° horizontal resolution) that uses turbulence parameterization based on the Boussinesq hypothesis and Prandtl's mixing length model. The data from the high-resolution model will also be used to check if the assumptions behind Prandtl's mixing length model are applicable to oceanography.

Knowing if this parameterization of turbulence produces reliable results is important, since coarse-resolution ocean models are widely used in large-scale climate simulations to explain important heat transport processes [9]. For instance, the Community Earth System Model (CESM) uses a 1° horizontal resolution and parametrizes turbulence based on Prandtl's mixing length model [1].

Chapter 1 describes how the spectrum of oceanic length scales makes it virtually impossible to build an ocean model that resolves all relevant length scales present in the ocean. Following this is a description of the turbulence closure problem, which states that small-scale flow does indeed influence the mean flow significantly. The Boussinesq hypothesis and Prandtl's mixing length model, which parameterize the turbulence via the mean flow, are then introduced. A selection of geophysical flow phenomena are introduced as well.

Chapter 2 contains a description of the setups of the numerical models. The chapter also features a model validation section in which it is examined whether or not the model produces reliable results that are consistent with geophysical theory, and whether or not the model has converged numerically during the spin-up period. This is done in order to test whether or not the results from the model are reliable when they are used for investigating whether or not Prandtl's mixing length model is applicable to oceanography.

In chapter 3, the data collected after the spin-up period are presented. The results include time-averaged representations of the flow of the numerical setups, which will be used to evaluate the characteristic differences between the high- and coarse resolution setups. Turbulence maps, mean flow velocity shear maps, and an analysis of the characteristic turbulent length- and velocity scales present within the flow are presented in this section as well. This will be used to examine whether or not Prandtl's mixing length model is applicable to oceanic flows.

Finally, in chapter 4, the results of the present thesis will be used to explain some of the findings in Lévy et al (2010) [6], and the significance of the present results with respect to ocean- and climate modelling will be discussed.

1.2 Oceanic length scales and numerical limitations

In order for a discrete, numerical ocean model to produce results that are useful in a large-scale climate model, the model must ideally capture all relevant dynamics of the flow. This means that the spatial grid spacing should be on the order of the smallest scale spatial fluctuations. Further, the

time step should be shorter than the inverse of the highest-frequency, temporal fluctuations.

In a study by Stammer [10] using satellite data, a spectral analysis has shown that a continuous spectrum exists in the ocean for all wavenumbers between $(10km)^{-1}$ and $(1000km)^{-1}$, which corresponds to the entire investigated range of wavenumbers in that paper. However, even very small-scale, high-frequency surface gravity waves on the scale of a few meters may impact the mean flow by e.g. Stokes drift, which is the phenomenon that small surface gravity waves lead to a non-zero mean transport. In a study by Bremer and Breivik [3], the authors note that one must be able to measure the wavelength spectrum down to scales of $20m$ in order to properly estimate the Stokes drift

Thus, there is an enormous range of length scales that need to be resolved in the ocean. Due to computational limitations, it is not practically possible to build a global ocean model with a mesh fine enough to capture all relevant length scales. The goal of the CESM is to develop a model using a 0.1° horizontal resolution [1]. While this resolution would capture most oceanic waves, it fails to capture sub-mesoscale waves, eddies, and turbulence that is indeed present in the ocean. This is the reason why understanding turbulence parameterization is an important part of ocean modelling.

1.3 Reynolds averaging and the turbulence closure problem

While the small-scale fluctuations might be present in the ocean, the practically relevant phenomena are typically long-term averages such as the general heat transport [9]. Therefore, even if computing power limits the ability to resolve all length scales, it might be possible to produce meaningful ocean models if the small-scale fluctuations do not affect the mean flow or can be parameterized via the mean flow. Therefore, we must examine how the mean flow is influenced by small-scale fluctuations. To do so, we divide the physical terms of the Navier-Stokes equations into a slowly-varying mean part denoted by capital letters and overbars and a fluctuating part denoted by primes:

$$u_i = U_i + u'_i, \quad p = P + p', \quad \rho = \bar{\rho} + \rho', \quad (1)$$

where u_i are the velocity vector components, p is the pressure, and ρ is the density. Under the Boussinesq approximation, temporal density changes are small relative to the spatial velocity gradient,

$$\frac{1}{\rho} \frac{D\rho}{Dt} \ll \frac{\partial u_i}{\partial x_i}, \quad (2)$$

where x_i are the coordinate vector components and t is time. This is usually true for oceanic flows [5, Chap. 4], so Navier-Stokes equations simplify to

$$\frac{\partial u_i}{\partial t} + u_j \frac{\partial u_i}{\partial x_j} = -\frac{1}{\rho_0} \frac{\partial p}{\partial x_i} + \frac{\rho - \rho_0}{\rho_0} g_j + \nu \frac{\partial^2 u_i}{\partial x_j^2}, \quad (3)$$

where ρ_0 is the hydrostatic density, ν is the kinematic viscosity, and g_j is the j 'th component of the field force. Note that the Navier Stokes equations are written in Einstein notation. Substituting the division into mean- and fluctuating parts from equation 1 into equation 3 and time-averaging yields

the Reynolds-averaged Navier-Stokes equations.

$$\frac{\partial U_i}{\partial t} + U_j \frac{\partial U_i}{\partial x_j} = -\frac{1}{\rho_0} \frac{\partial P}{\partial x_i} + \frac{\bar{\rho} - \rho_0}{\rho_0} g_i + \frac{\partial}{\partial x_j} \left(\nu \left[\frac{\partial U_i}{\partial x_j} + \frac{\partial U_j}{\partial x_i} \right] - \overline{u'_j u'_i} \right), \quad (4)$$

where we have used that the time-average of a fluctuating part is zero. What is remarkable about this result is that the mean flow is governed in part by small-scale fluctuations through the mean of an unsteady term, $-\overline{u'_j u'_i}$. This term is known as Reynolds stress and is generally non-zero, which means that in order to predict the mean flow, one must in principle solve all small-scale fluctuations.

This presents a challenge to modern fluid mechanics simulation problems because the grid spacing imposes a lower boundary on the length scales of small-scale turbulence that can be resolved in the model. Any sub-grid scale turbulence will therefore impact the mean flow in a way that is impossible to predict. This challenge is known as the turbulence closure problem.

1.4 The Boussinesq hypothesis and Prandtl's mixing length model

Many attempts have been made to model the Reynolds stress without actually having to resolve all length scales. That is, closing the turbulence by relating the Reynolds stress to the mean flow. A turbulence closure model that has found widespread use is the Boussinesq hypothesis, which states this turbulence may be modeled through a turbulent viscosity, ν_T , and a (assumed constant) turbulent kinetic energy, \bar{e} [5, Chap. 12],

$$\overline{u'_i u'_j} = \frac{2}{3} \bar{e} \delta_{ij} - \nu_T \left(\frac{\partial U_i}{\partial x_j} + \frac{\partial U_j}{\partial x_i} \right), \quad \bar{e} = \frac{1}{2} \mathbf{u}'^2. \quad (5)$$

This is a practical hypothesis since it is a simple parameterization of the turbulence based on the mean flow through the substitution of the molecular viscosity ν with the effective viscosity $\nu + \nu_T$ and the addition of a constant term. It now remains to find reasonable values of the turbulent viscosity, ν_T , and the turbulent kinetic energy, \bar{e} . These values are generally found in an empirical manner in which the values are tuned in order for the model to produce realistic results rather than being based on physical principles.

Based on a dimensional analysis, Prandtl's mixing length model assumes that the turbulent friction can be interpreted as $\nu_T = l_T u_T$, where l_T is a characteristic turbulent length scale and u_T is a characteristic turbulent velocity scale [5, Chap. 12]. For two-dimensional, unidirectional shear flows, this is usually expressed by evaluating the $u_i = u, u_j = v$ term in equation 5.

$$-\overline{u'v'} = \nu_T \frac{dV}{dx} = l_T u_T \frac{dV}{dx} \quad (6)$$

This may be generalized to a mean flow that is not unidirectional by inserting x, y, U , and V into equation 5 along with Prandtl's assumption that $\nu_T = l_T u_T$:

$$-\overline{u'v'} = l_T u_T \left(\frac{dV}{dx} + \frac{dU}{dy} \right) \quad (7)$$

The main purpose of the present thesis is to examine whether or not the formulation of the Boussinesq approximation and Prandtl's hypothesis stated in equation 7 is valid for the numerical models developed in the present project.

1.5 Sverdrup's balance

Sverdrup's balance describes the mean flow in the interior of the ocean. This balance provides a good estimate at the observed meridional transport in the North Atlantic Ocean [8, Chap. 1].

The velocity of this mean flow is on the order of 1cm/s and varies over a length scale of thousands of kilometers [8, Chap. 1]. Thus, the Rossby number $R_o = U/fL \ll 1$, which means that the non-linear acceleration term of the Navier-Stokes equation is much smaller than the Coriolis acceleration term except in regions close to the equator [5, Chap. 11]. For flows in which several length scales are to be resolved, it is useful to model the turbulent effect on the mean flow through a turbulent viscosity, ν_T (see chapter 1.4). It has been shown numerically that in the interior of the ocean, where mean velocity gradients are small, the horizontal turbulent viscosity, $\nu_{T,H}$, is small, such that the horizontal Ekman number $E_H = \frac{\nu_{T,H}}{fL^2} \ll 1$. Thus, the horizontal turbulent viscosity may be ignored [5, Chap. 11]. Further assuming that the flow is incompressible, that density variations are small, and that effects of vertical turbulent viscosity are limited to the upper, mixed layer, it can be shown that [8, Chap. 1]

$$\beta V_S \equiv \beta \int_{-D}^0 v dz = \hat{\mathbf{z}} \cdot \nabla \times \left(\frac{\boldsymbol{\tau}}{\rho_0} \right). \quad (8)$$

Here, β is the meridional gradient of the Coriolis acceleration, the vertical coordinates $z = -D$ and $z = 0$ refer to the bottom and surface of the ocean, respectively, and $\boldsymbol{\tau}$ is the surface wind stress.

Equation 8 is known as Sverdrup's balance and presents a remarkable result as it predicts the general equator-ward flow in the interior of the ocean. Since Sverdrup's balance is robust and experimentally backed [8, Chap. 1], it will be used in the present thesis to validate the numerical setup. That is, it will be checked if the present numerical models satisfy Sverdrup's balance to first order. If they do, it is an indication that the numerical models produce reliable results.

1.6 Gyres and western boundary currents

Sverdrup's balance presents a problem in closed basins since it predicts a constant meridional flow throughout the basin for a zonally constant wind forcing. At the northern and southern boundaries, this conflicts with the boundary condition that the velocity is parallel to the boundary.

This problem has prompted the development of homogenous models, which assume that viscous effects are limited to the mixed layer and a bottom boundary layer, such that there is no vertical shear in the interior. In this approximation, the flow in the interior can then be represented by a streamfunction, ψ . Assuming that the flow is geostrophically balanced, that nonlinear effects are negligible, and that turbulence may be modeled by turbulent viscosity (see section 1.4), this reproduces Sverdrup's balance in the interior [8, Chap. 2].

For zonally constant wind stresses, Sverdrup's balance implies that the streamfunction continuously increases or decreases throughout the zonal extent of the basin depending on the sign of $\hat{\mathbf{z}} \cdot \nabla \times \boldsymbol{\tau}$ in equation 8. Imposing the boundary condition stating that the flow is tangential to the boundary at the boundary implies that the streamfunction must be constant along the boundaries. Trusting that Sverdrup's balance is a good description of the interior flow, this means that the value of the streamfunction must change sharply close to the boundary, resulting in a strong boundary current. It can be shown that this sharp change only happens at the western zonal boundary, resulting in a

western boundary current [7].

Since $\beta > 0$ everywhere on Earth, the sign of $\hat{\mathbf{z}} \cdot \nabla \times \boldsymbol{\tau}$ determines the direction of the Sverdrup transport. Thus, when wind is blowing from east to west in the part of the basin closest to the pole and from west to east in the part closest to the equator, the general Sverdrup transport is directed toward the equator, and the western boundary current is poleward. This circulation is known as a subtropical gyre. When the wind is blowing from west to east near the pole and east to west near the equator, the Sverdrup transport is poleward, and the western boundary current is equatorward. This is known as a subpolar gyre [8, Chap. 2].

Western boundary currents such as the Gulfstream are responsible for much of Earth's heat transport [9]. Therefore, accurately predicting the characteristics of western boundary currents is an important feature of ocean models used in climate models. The structural difference of the western boundary current between high-resolution and coarse-resolution models will be investigated in the present thesis.

When a numerical ocean model is released, the western boundary current takes some time to reach a steady state that represents a physically realistic situation. In the present thesis, the strength of the western boundary current will serve as a validation parameter to check if the models have converged numerically.

1.7 Analyzing discrete ocean model results

The numerical model used in the present thesis returns spatially and temporally discrete data. The data collected are snapshots of instantaneous values. Based on this snapshot data, time-averages of variables can be computed. This is used to divide the flow into a time-averaged, steady part, and an unsteady part. This is the same division as done for the Reynolds averaging of the Navier Stokes equations (equation 1), where $U_i = \overline{u_i}$ is the time-average of u_i , and $u'_i = u_i - U_i$, and u_i is the snapshot velocity. This leaves u'_i as the turbulent velocity. For simplicity, we now introduce the notation $u_x = u$; $u_y = v$; and $u_z = w$. At each snapshot, the horizontal volume transport, (u_S, v_S) , is defined as a depth integral of the horizontal velocity. For the discrete results of a numerical model, the integral is replaced by a discrete sum,

$$u_S = \int_{-D}^0 u dz = \sum_{k=0}^N u_k \Delta z_k; \quad v_S = \int_{-D}^0 v dz = \sum_{k=0}^N v_k \Delta z_k, \quad (9)$$

where k is the index of the vertical grid cell considered. A streamfunction ψ may now be defined via the relation

$$u_S = \frac{\partial \psi}{\partial y} = \frac{\psi_{j+1} - \psi_{j-1}}{2\Delta y}; \quad v_S = -\frac{\partial \psi}{\partial x} = \frac{\psi_{i+1} - \psi_{i-1}}{2\Delta x}, \quad (10)$$

where the continuous differentiation operator has been replaced by its discrete representation [5, Chap. 6]. In equation 10, i and j are the indices of the discrete x - and y coordinates, respectively. A time-averaged streamfunction $\Psi = \overline{\psi}$ can then be used to describe the mean volume transport.

The separation into mean- and fluctuating parts allows us to use u' and v' to compute $u'v'$ at each grid cell and time step. Time-averaging this data yields the unsteady term $\overline{u'v'}$ from the Reynolds-averaged Navier-Stokes equations (equation 4). This serves as a measure of the horizontal turbulence

in the model. In order to produce a two-dimensional image of this data, a depth integral, $(\overline{u'v'})_S$ of the unsteady term can be used.

$$(\overline{u'v'})_S \equiv \int_{-D}^0 \overline{u'v'} dz = \sum_{k=0}^N \overline{u'_k v'_k} \Delta z_k, \quad (11)$$

Another measure of the horizontal turbulence is the turbulent horizontal transport, $|\mathbf{u}'_S|$. This is defined as a depth integral of the horizontal turbulent speed from the bottom to the sea surface.

$$|\mathbf{u}'_S| \equiv \int_{-D}^0 \sqrt{u'^2 + v'^2} dz = \sum_{k=0}^N \sqrt{u_k'^2 + v_k'^2} \Delta z_k, \quad (12)$$

Using equation 12, the turbulent horizontal transport can be calculated for each grid cell at each time step. The time-average of this data, $|\overline{\mathbf{u}'_S}|$, and the depth-integrated turbulent term, $(\overline{u'v'})_S$, present images of the areas in the basin where turbulence generally plays a significant role.

Using the discrete approximation to the differential operator, the mean flow shear can be calculated. Again, a discrete depth-integral of the data can be used to present a two-dimensional image of the data.

$$\frac{dV}{dx} = \frac{V_{i+1} - V_{i-1}}{2\Delta x}; \quad \left(\frac{dV}{dx}\right)_S = \sum_{k=0}^N \frac{dV}{dx} \Delta z_k, \quad (13)$$

where i is the index of the zonal grid cell considered. dU/dy is computed in a similar manner. Using the horizontal images of the vertically integrated data, $(\overline{u'v'})_S$, $|\overline{\mathbf{u}'_S}|$, and $(dV/dx)_S$ and $(dU/dy)_S$, it can be checked if Prandtl's mixing length model predicts turbulence in areas where turbulence is actually present. It can also be checked whether Prandtl's assumed the linear correlation between the non-vertically integrated data $\overline{u'v'}$ and $dU/dy + dV/dx$ is generally appropriate.

Assuming that any characteristic turbulent length scale is reflected in the turbulent transport, $|\mathbf{u}'_S|$, the term l_T in equation 7 can be estimated based on Fourier transforms of cross sections of $|\mathbf{u}'_S|$. These Fourier transforms must be based on snapshot data rather than time-average data, since the instantaneous, turbulent structure is smeared out in averaged data. The resulting power spectra may then be time-averaged in order to describe the general structure of the flow. Any characteristic wavenumber will then be the inverse of a characteristic wavelength, or length scale. A characteristic turbulent velocity scale may be estimated as the mean horizontal turbulent speed, $|\mathbf{u}_h| = \sqrt{u'^2 + v'^2}$, over all grid cells. If the turbulent speed is binned, it may also be estimated as the most frequent turbulent speed. The horizontal speed is used because only horizontal turbulence is represented in equation 7. Based on the turbulent length- and velocity scales, the turbulent viscosity $\nu_T = u_T l_T$ can be estimated, and it can be checked whether or not any linear correlation between $\overline{u'v'}$ and $dU/dy + dV/dx$ has a slope comparable to the estimate of ν_T as assumed by Prandtl's mixing length model.

2 Model setup

2.1 Versatile Ocean Simulator (VEROS)

In order to perform the numerical experiments described in the present thesis, the Versatile Ocean Simulator (VEROS) has been used. VEROS is developed by the Veros Team at the Niels Bohr Institute, University of Copenhagen and is an adaptation of python Ocean Model 2 (pyOM2) v2.1.0 developed by Institut für Meereskunde, Hamburg University. The main difference is that while pyOM2 relies on a Fortran backend, VEROS runs in pure Python.

VEROS and pyOM2 are based on the Navier-Stokes equations simplified under the Boussinesq approximation (equation 3) and the incompressible continuity equation $\nabla \cdot \mathbf{u} = 0$. The governing equations of motion are evaluated in a pseudo-cartesian coordinate system in which the zonal coordinate x refers to the longitude, and the meridional coordinate y refers to longitude, and the vertical coordinate z refers to depth into the water column. The continuous equations of motion are discretized on an Arakawa C-grid. Please refer to the VEROS documentation available at <https://veros.readthedocs.io/en/latest/> for further information.

2.2 Model domain, forcings, and model setup

For the present project, a numerical model has been made based on the VEROS Navier-Stokes equation solver. The present model is an idealized setup featuring a topographically flat seabed with a depth of 5000m and vertical boundaries on the northern hemishphire of a globe similar to Earth. The basin spans from 20°N to 40°N and features a 30° east-west extent. This location and basin size corresponds roughly to the North Atlantic Ocean. The model uses free-slip, no normal flow boundary conditions. The model uses a realistic representation of the Coriolis frequency computed for each grid cell as

$$f = 2\Omega \sin(\phi) = 2\Omega \sin\left(\frac{\pi}{180^\circ}y\right), \quad (14)$$

where y is the meridional coordinate measured in degrees. The surface heat flux into the top grid cell measured in °C/s is calculated as

$$q = T_R (T_A - T_S), \quad (15)$$

where T_S is the sea surface temperature, $T_R = 8.17 \times 10^{-7} s^{-1}$ is the inverse of a characteristic time scale. T_A is the atmospheric temperature,

$$T_A = T_{A,0} \left(1 - \frac{y - y_0}{L_y}\right), \quad (16)$$

where $T_0 = 15^\circ C$, $y_0 = 20^\circ N$ is the meridional origin located in the south-west corner of the basin, and $L_y = 20^\circ$ is the meridional extent of the basin.

Using this basin, four different experimental setups have been examined representing two physically different systems: a subtropical gyre and a subpolar gyre. In both cases, the zonal wind stress

has the form of one half period of a harmonic wave, and its meridional component is zero:

$$\boldsymbol{\tau}_P = \Gamma \cos \left[\frac{\pi (y - y_0)}{L_y} \right] \hat{\boldsymbol{x}}; \quad \boldsymbol{\tau}_T = -\Gamma \cos \left[\frac{\pi (y - y_0)}{L_y} \right] \hat{\boldsymbol{x}}, \quad (17)$$

where the subscripts P and T denote the subpolar- and subtropical gyre models, respectively, and $\Gamma = 0.1N/m^2$.

For both the subpolar and the subtropical gyre, a high-resolution and a coarse-resolution model has been configured for the purpose of this project. The high-resolution models feature a horizontal resolution of 0.1° corresponding to the goal for the CESM ocean model, while the coarse-resolution models feature 1° resolution corresponding to the current state of the CESM ocean model. Both models feature 70 vertical layers. The layer thickness increases progressively from 2.12m near the surface to 217m near the bottom of the basin. The high-resolution models use biharmonic friction, while the coarse-resolution models use horizontal friction to parameterize turbulence. The full settings may be found in appendix A.3.

2.3 Model initiation and data collection

The model is released with initial conditions that do not represent a physically realistic steady state. The fluid is initially at rest with a uniform salinity of $35g/kg$ and a temperature that varies linearly from $15^\circ C$ at the surface to $0^\circ C$ at the bottom. Due to these non-physical initial conditions, the model should run until it converges to a physically plausible steady state before experimental data is collected. This is known as the spin-up period. During the spin-up period, instantaneous snapshot data is collected every ten days of model time. These snapshots are used to compute window averages of certain parameters every 180 days of model time. This data will not be used to investigate the properties of the flow since the spin-up data represents physically unrealistic flow. Rather, the spin-up data will be used to check if the model has converged to a steady state during the spin-up period.

In the present numerical models, a 20 model year spin-up period has been used. After the spin-up period, experimental data is collected for one model year. In this period, instantaneous snapshots are collected every three model days. This data will be used for analyzing the flow characteristics and examining Prandtl's mixing length model.

3 Results

3.1 Model validation

3.1.1 Spin-up analysis

The window averages computed during the spin-up period is used in this section to determine whether or not the numerical model has converged to a steady state. The parameter examined here is the strength of the western boundary current, defined as the meridional volume flux between $0^\circ E$ and $5^\circ E$ for the coarse-resolution models, and between $0^\circ E$ and $0.5^\circ E$ for the high-resolution models.

$$V_{S,WBC} = \left| \int_{z=-D}^{z=0} \int_{x=0^\circ E}^{x=x_0} V dx dz \right| \quad (18)$$

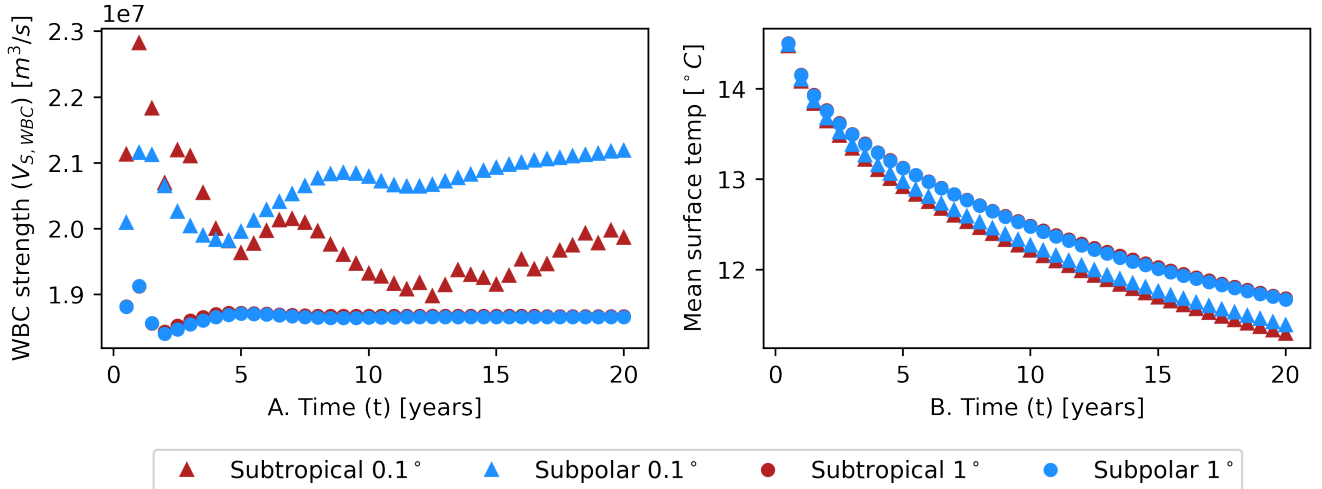


Figure 1: Development of the western boundary current strength (WBC) and the mean sea surface temperature during the spin-up phase of the models.

where V is the 180 day window averages of v , and $x_0 = 5^\circ E$ and $x_0 = 0.5^\circ E$ for the low- and high-resolution models, respectively. The absolute value of the integral is used in order to evaluate the strength rather than the direction of the western boundary current. Note that the integral has been evaluated using its discrete representation as demonstrated several times in section 1.7. In figure 1A, the strength of boundary current is shown as a function of time for the four numerical setups.

For the low-resolution models, the strength of the western boundary current stabilizes after roughly 8 years of integration. Note that the stable strength of the western boundary current is practically identical for the subpolar and the subtropical gyre. For the high-resolution setups, the western boundary current strength does not reach a constant level during the 20 year spin-up period. The strength of the western boundary current must reflect the magnitude of the interior flow. As shown in section 3.1.2, the high-resolution models satisfy Sverdrup’s balance. This means that the western boundary currents must have magnitudes that closely resemble realistic physical flows. This combined with the fact that the slope is decreasing at the end of the spin-up period in figure 1A indicates that the strength of the western boundary current has reached a near-steady state where it slowly and monotonously approaches its steady state value.

Figure 1B shows the mean sea surface temperature during the 20 year spin-up period. This shows that the temperature is relatively far from reaching a steady state at the time of data collection. This is not necessarily problematic since the relevant data for this project is not strictly temperature-related. However, temperature changes can lead to slight density changes, which influences the flow velocity. Thus, the flow field reported in this thesis might change slightly if the model were allowed to reach a steady temperature.

3.1.2 Checking the general circulation

In order to check whether the model produces physically meaningful results, it is checked if the interior flow of the models satisfy Sverdrup’s balance (equation 8). For the wind stress specified in equation 17, this predicts a near-sinusoidal meridional transport. Using the post-spin-up data, the time-average meridional transport V_S of v_S (see equation 9) has been computed for each horizontal

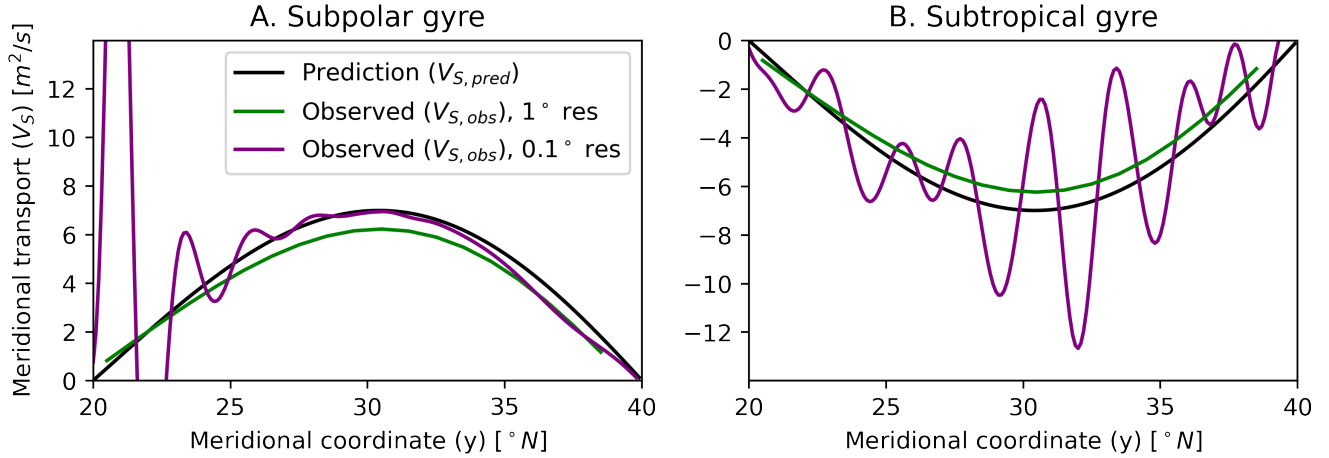


Figure 2: Cross section at $x = 20^\circ E$ showing the average observed meridional transport as a function of latitude as well as the predicted transport using Sverdrup’s balance.

grid cell.

In figure 2, the predicted meridional transport and the observed meridional transport is shown for a meridional cross section located in the interior at $x = 20^\circ E$ where Sverdrup’s balance is expected to apply. For this cross section, it appears that the observed order of the meridional transport satisfies Sverdrup’s balance for all model setups. Note that for the high-resolution, subtropical model, powerful fluctuations are present, which represent temporally stable turbulence. However, the observed transport fluctuates around the predicted value.

Figure 2 only represents a cross section at a single zonal coordinate. Figures 3A-D presents for each horizontal grid cell the difference $V_{S,rel}$ between the observed transport and the predicted transport normalized by the predicted transport.

$$V_{S,rel} = \frac{V_{S,obs} - V_{S,pred}}{V_{S,pred}}. \quad (19)$$

If the model satisfies Sverdrup’s balance, $V_{S,rel}$ should be close to zero in the interior of the basin. It is clear from figures 3A and 3B, which show $V_{S,rel}$ for the subpolar- and subtropical coarse-resolution models, that $V_{S,rel}$ is generally close to zero in the interior of the domain. For the high-resolution subpolar gyre model in figure 3C, $V_{S,rel}$ is very close to zero in the center of the basin. For the high-resolution subtropical gyre model in figure 3D, $V_{S,rel}$ is generally non-zero in the center. However, it is not systematically positive or negative, but rather varies randomly around zero, which indicates that this reflects stationary turbulence rather than a mismatch between the predicted and observed meridional transport. This indicates that all models perform as intended and produce physically meaningful output.

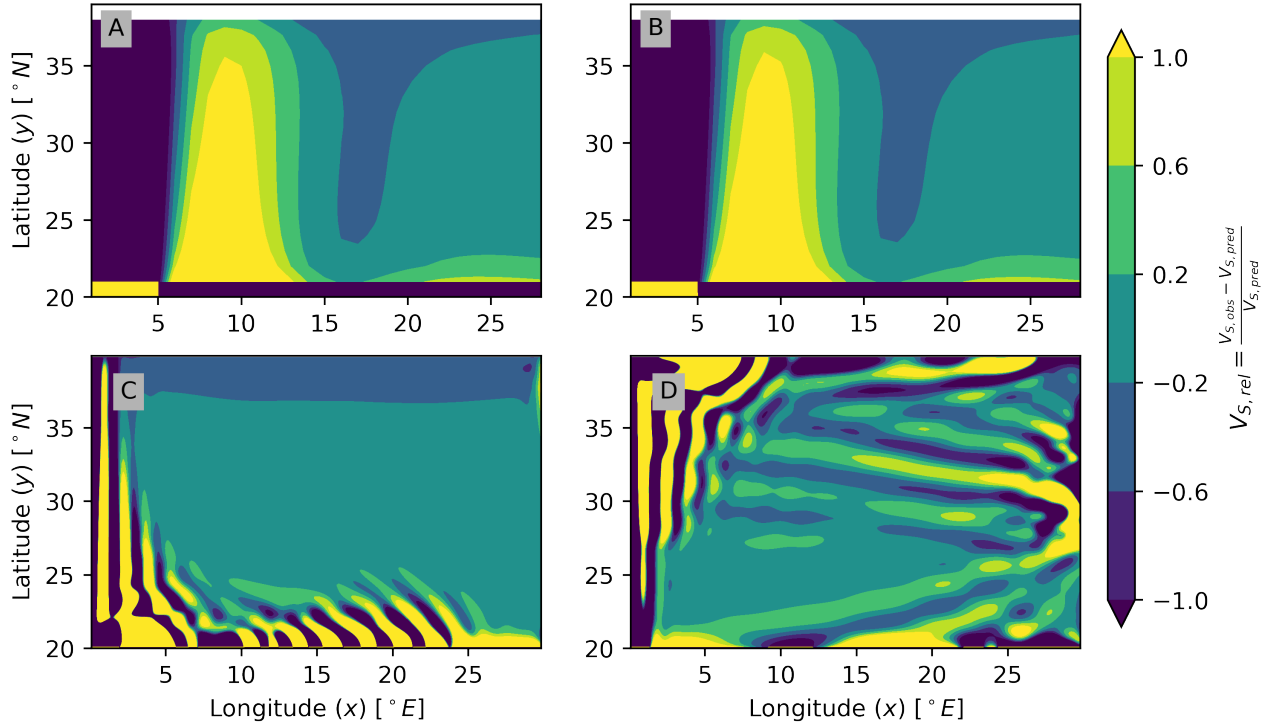


Figure 3: Plot showing the difference $V_{S,rel}$ between the observed $V_{S,obs}$ and predicted $V_{S,pred}$ meridional transport normalized by the predicted meridional transport. A) subpolar, low resolution. B) Subtropical, low resolution. C) Subpolar, high resolution. D) Subtropical, high resolution.

3.2 General characteristics of the gyres

3.2.1 Mean, interior flow

The streamfunction computed via equation 10 presents a two-dimensional image of the basin where the streamlines of the depth-integrated flow are parallel to the contours of the streamfunction. Thus, the average streamfunction Ψ represents the mean volume transport. The average streamfunctions of the four model setups are shown in figures 4A-D.

Figures 4C and 4D, which show the coarse-resolution subtropical- and subpolar gyres, respectively, indicate that the coarse-resolution models do not predict any structural differences between the subpolar gyre and the subtropical gyre, which is also indicated in figures 3A-B. The high-resolution subtropical gyre predicts significant, temporally stable flow structure in the center of the domain, which the coarse-resolution model fails to capture. However, the high-resolution subpolar gyre in figure 4B has a very similar structure to its low-resolution counterpart except near the southern boundary, where turbulence is dominant (see section 3.2.3).

3.2.2 Western boundary current

The extent and structure of the western boundary current is significantly different for the high- and coarse-resolution setups. As shown in figures 3A-B, the coarse-resolution models predict only one

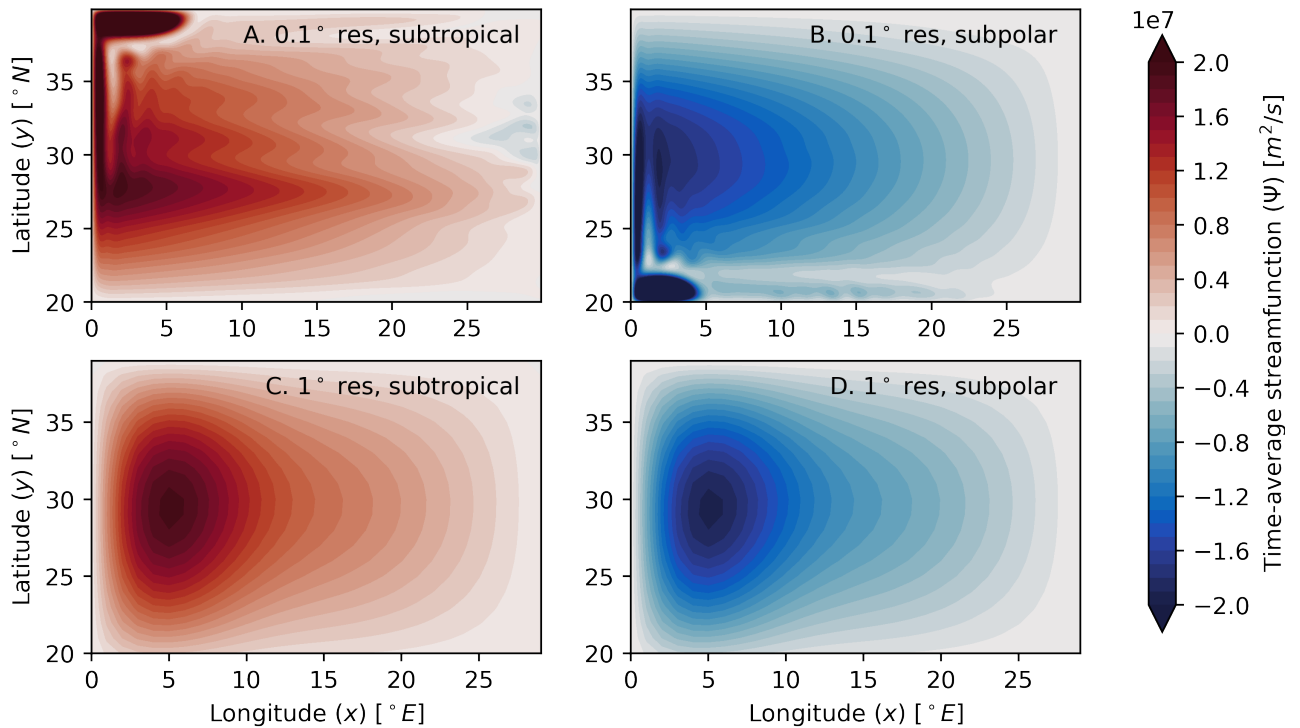


Figure 4: Time-averaged stream functions Ψ for all models. "res" is short for resolution

node of a main current from $0^\circ E$ to $5^\circ E$ and a recirculation from $5^\circ E$ to $12^\circ E$. Here, a main current describes a current antiparallel to Sverdrup's balance, and a recirculation describes a current parallel to, but significantly larger than, Sverdrup's balance. For the high-resolution models, several nodes of a main current and a recirculation are present, and the number of nodes changes throughout the meridional extent of the basin. Assuming that the high-resolution models produces the best results, the coarse-resolution models fail to predict the structure of the western boundary current.

3.2.3 Turbulence

The coarse-resolution models do not feature turbulence, since the resolution is too low and the turbulent friction is too high. Thus, the following analysis of observed turbulence is based on data from the high-resolution models only.

The average turbulent horizontal transport, $\overline{|\mathbf{u}'_S|}$, and the the depth-integral of the unsteady term of the Reynolds averaged Navier-Stokes equations, $\overline{(u'v')}_S$, have been computed for each horizontal grid cell using equations 12 and 11, respectively, based on the data collected after the spin-up period. Figures 5A and 5B show $\overline{|\mathbf{u}'_S|}$ for the subtropical- and subpolar high-resolution models, respectively, and figures 5C and 5D show $\overline{(u'v')}_S$ for the subtropical- and subpolar high-resolution models, respectively. Both of these representations of turbulence predict that the subtropical gyre features turbulence in the northern part of the western boundary current and in the eastern part of the basin, while the subpolar gyre features turbulence near the southern boundary.

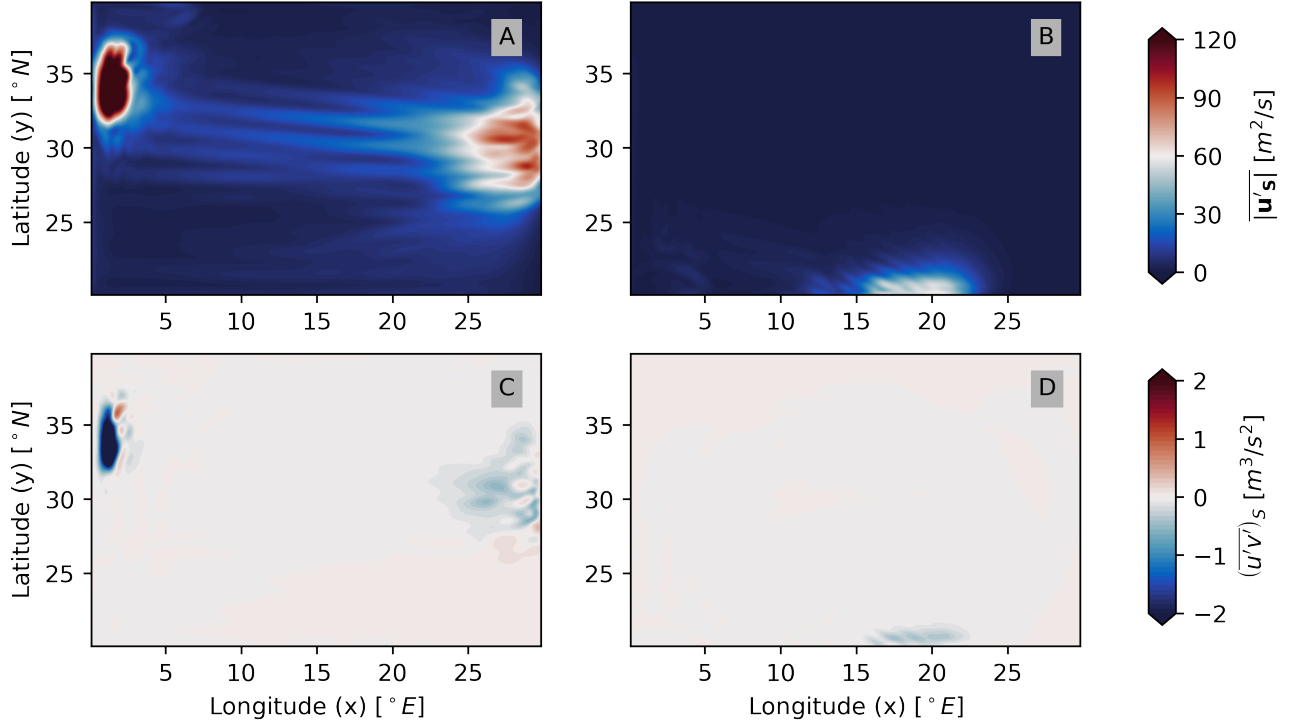


Figure 5: Turbulent transport speed $|\overline{\mathbf{u}'_s}|$ (A and B) and depth-integrated unsteady term $(\overline{u'v'})_s$ (C and D) for the high-resolution subtropical gyre (A and C) and subpolar gyre (B and D).

3.3 Characteristic length scales

Prandtl's mixing length model solves the turbulence closure problem based on the assumption that a turbulent viscosity is the product of characteristic turbulent length- and velocity scales of the flow. This implies the existence of such scales.

In accordance with the procedure described in section 1.7, Fourier transforms of the horizontal turbulent transport, $|\mathbf{u}'_s|$, have been made for meridional cross sections at all discrete zonal grid coordinates at each time step. These spectra have been normalized by scaling each spectrum with the inverse of its maximum value. An example of such a cross section and a resulting normalized power spectrum is shown in appendix A.2. The time-average of these power spectra of wavenumbers is shown in figure 6A for the subpolar gyre and in figure 6C for the subtropical gyre as functions of longitude. The same analysis has been carried out for zonal cross sections at all discrete meridional coordinates. The resulting power spectrum of wavenumbers is shown in figures 6B for the subpolar gyre and 6D for the subtropical gyre as functions of latitude.

All spectra in figures 6A-D show that very low frequencies corresponding to long length scales are significant. Since in the present project we look for small-scale turbulence, these low-frequency signals are disregarded. The subpolar gyre features a turbulent area near its southern boundary from $14^\circ E$ to $23^\circ E$ and $20^\circ N$ to $22^\circ N$. In this area, figure 6B shows a nonzero signal at a zonal wavenumber of $k \sim (0.7 \pm 0.2)^\circ E^{-1}$, corresponding to a characteristic length scale of $(1.4 \pm 0.4)^\circ N = (150 \pm 40) km$. Such a clear signal is absent in the relevant area from $14^\circ E$ to $23^\circ E$ of figure 6A. For the subtropical

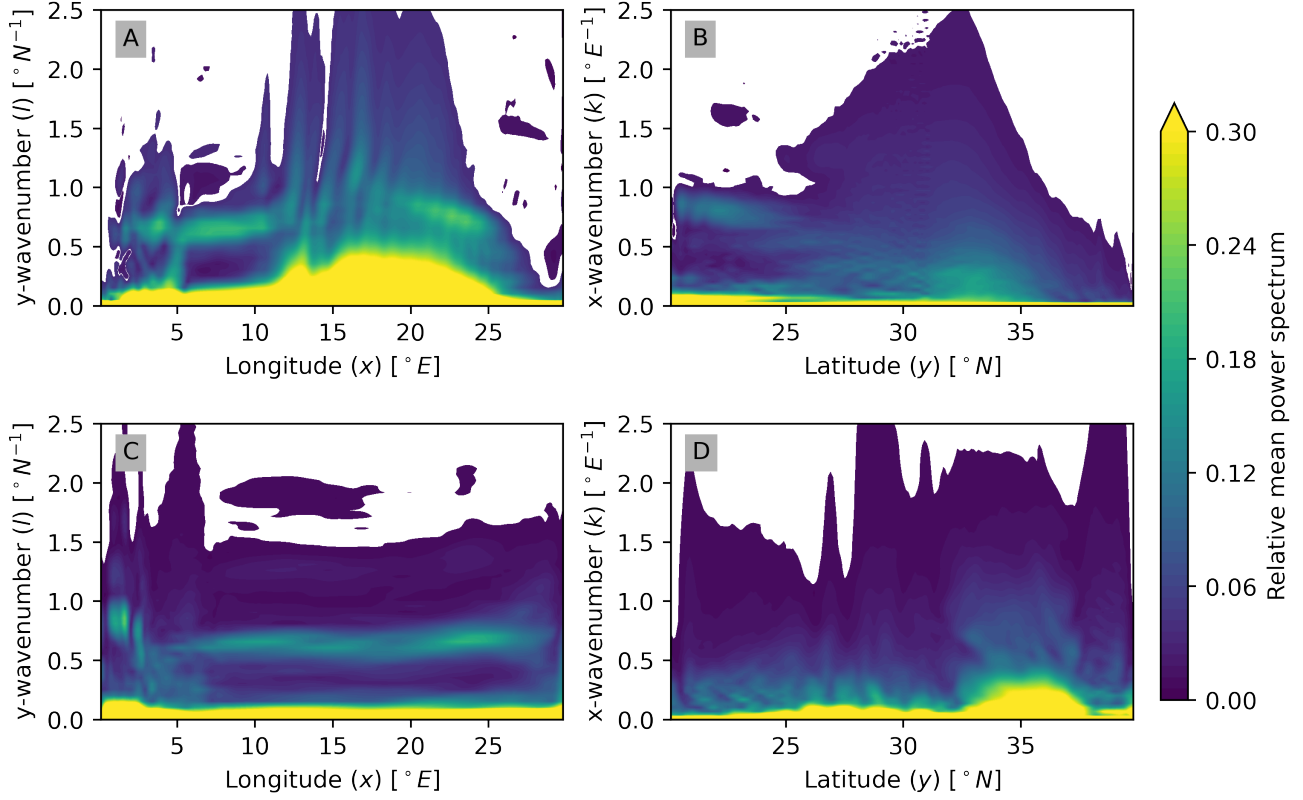


Figure 6: Time-averaged power spectra of the turbulent transport $|\overline{\mathbf{u}_s}|$ based on cross sections at the locations indicated on the x -axes. A and B show data for the subpolar gyre, and C and D show data for the subtropical gyre

gyre, a clear signal is absent as well for the zonal wavenumber spectrum in figure 6D. However, figure 6A shows that in the western turbulent area from $0.4^\circ E$ to $3^\circ E$ and from $31^\circ N$ to $37^\circ N$, a characteristic meridional wavenumber of $l \sim (0.8 \pm 0.2)^\circ N^{-1}$ corresponding to a length scale of $(1.3 \pm 0.3)^\circ N = (140 \pm 30)km$ is present. In the eastern boundary turbulent area from $23^\circ E$ to $30^\circ E$ and $25^\circ N$ to $35^\circ N$, a signal is present at $l \sim (0.7 \pm 0.3)^\circ N^{-1}$, corresponding to a length scale of $(1.4 \pm 0.6)^\circ N = (160 \pm 70)km$. These length scales agree within their uncertainties, and the best estimate at a general turbulent length scale is $(150 \pm 30)km$. This shows that a characteristic length scale is indeed present in the models, and this length is constant to first order. In this section, I have estimated the errors using the signal width in figures 6A-D and propagated the errors [2].

Note that even though the length scales agree within uncertainties, the characteristic length scale in the western boundary current of the subtropical gyre in figure 6C is notably shorter than that in the interior of the gyre. This may be a reflection of the law of the wall, which states that the turbulent velocity generally decreases near a wall [4]. If this is true and the characteristic length scale decreases due to a decrease in turbulent velocity, this might indicate that a characteristic time scale $t_T = l_T/u_T$ exists, which is constant throughout the basin.

3.4 Characteristic velocity scale

The turbulent characteristic velocity scale has been estimated as the mean horizontal turbulent speed and as the most frequent horizontal speed, based on measurements of the horizontal turbulent speed $|\mathbf{u}_h|$ (see section 1.7) at each grid cell at each time step. The data has been binned in intervals of $2.5 \times 10^{-5} m/s$ in order to calculate the most frequent (ie. the mode of) speed at a $2.5 \times 10^{-5} m/s$ accuracy. Sorting this data by its vertical coordinate shows that the mean and mode turbulent speed is close to zero near the bottom of the domain and increases gradually toward the sea surface. For the subtropical gyre, the flow reaches a mean speed of $(36 \pm 3) \times 10^{-3} m/s$ and a mode of $(8.21 \pm 0.03) \times 10^{-3} m/s$ at the sea surface in the western boundary turbulent area, and a mean speed of $(21 \pm 2) \times 10^{-3} m/s$ and a mode of $(2.92 \pm 0.03) \times 10^{-3} m/s$ in the eastern boundary turbulent area. The southern turbulent area of the subpolar gyre features a surface mean velocity of $(9.2 \pm 0.6) \times 10^{-3} m/s$ and a mode of $(4.74 \pm 0.03) \times 10^{-3} m/s$. For plots of the histograms and the variation of the means of modes with depth, please refer to appendix A.1.

This analysis shows that a characteristic turbulent velocity is not well-defined for the domain since the mean and mode both vary with depth. Any turbulent viscosity $\nu_T = l_t u_T$ should therefore be depth-dependant, which is not the case for the coarse-resolution models presented in this report. It is also difficult to determine a characteristic velocity at any depth, since the two estimates produce inconsistent results. Thus, from the present analysis, it can only be concluded that the characteristic velocity is most likely less than the highest estimate of the characteristic velocity, which in all cases is the mean velocity.

3.5 Checking Prandtl's mixing length model

For each grid cell, the unsteady term, $\overline{u'v'}$, and the velocity shear, $dU/dy + dV/dx$, have been calculated as described in section 1.7. Using the results from section 3.3 and 3.4, the turbulent viscosity in each of the turbulent areas predicted by Prandtl's mixing length model becomes $\nu_{T,south} = l_T u_{T,south} \leq (1400 \pm 300) m^2/s$; $\nu_{T,west} = l_T u_{T,west} \leq (5400 \pm 1200) m^2/s$; and $\nu_{T,east} = l_T u_{T,east} \leq (3200 \pm 700) m^2/s$, where subscripts west and east refer to the turbulent areas of the subtropical gyre and subscript south refers to the turbulent area of the subpolar gyre. Note that the turbulent viscosity is less than some value because section 3.4 concluded that only an upper limit of u_T could be determined.

Figures 7A-C show scatter plots of $\overline{u'v'}$ as a function of $dU/dy + dV/dx$ for the three turbulent areas. In the plots, a black line represents Prandtl's mixing length model (equation 7) based on the highest estimates of u_T . This means that according to the mixing length model, most data points should satisfy

$$-\nu_T \left(\frac{dV}{dx} + \frac{dU}{dy} \right) \leq \overline{u'v'} \leq 0. \quad (20)$$

Examining figures 7A-C, this is generally not the case. However, in the turbulent areas of the subtropical gyre (7A and 7B), Pearson's correlation coefficient is $\rho_{west} = -0.27$ and $\rho_{east} = -0.20$, which indicates that $\overline{u'v'}$ is in fact negatively correlated with $dU/dy + dV/dx$. For the subpolar gyre, $\rho_{south} = 0.21$ is positive - contrary to the prediction of the mixing length model.

Thus, the mixing length model fails to properly describe the relation between $\overline{u'v'}$ and $dU/dy +$

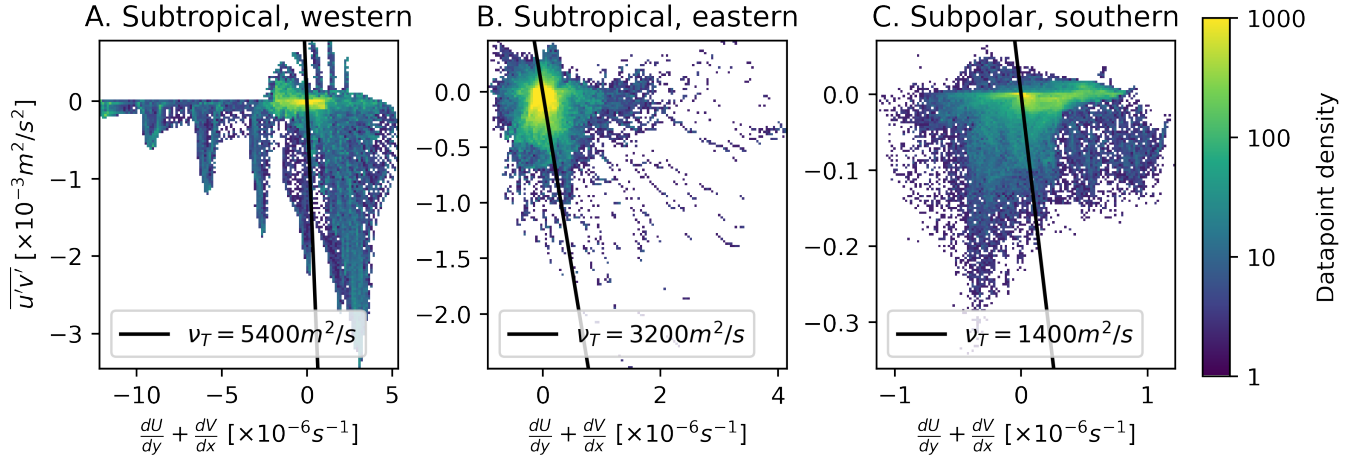


Figure 7: Scatter plots of the turbulent term $\overline{u'v'}$ as a function of the velocity shear $dU/dy + dV/dx$. The slope $-\nu_T$ of the black lines represents the estimate of the upper boundary on the turbulent viscosity based on the characteristic length- and velocity scale analyses.

dV/dx on a grid-cell basis in the high-resolution models.

The depth integrated velocity shear $(dU/dy + dV/dx)_S$ has been calculated using the form of equation 13. These results are shown in figures 8A, 8C, and 8B for the subtropical- and subpolar high-resolution models and for the coarse-resolution subtropical model, respectively. The coarse-resolution, subpolar results are not plotted because they are practically equal to the coarse-resolution, subtropical results except for a change of sign (this is reflected in figure 4C-D showing the streamfunction structure for the coarse-resolution models). The mixing length model assumes that the structure of the velocity shear in figures 8A-C is equal to the structure of the unsteady term in figures 5C-D. For the subtropical gyre, the coarse-resolution model predicts turbulence in a much larger area at the western boundary than what is observed. It falsely predicts weak turbulence between $6^\circ E$ and $15^\circ E$. This might be a reflection of the over-estimated width of the western boundary current and its recirculation. The model fails to predict turbulence at the eastern boundary. The high-resolution model shear predicts turbulence in a slightly larger area than observed at the western boundary, and it does predict some turbulence in the eastern turbulent area. However, it falsely predicts turbulence at the northern boundary as well as changes of signs of the turbulent term due to recirculation nodes in the western boundary current.

For the subpolar gyre, only the high-resolution model shear predicts turbulence at the observed southern turbulent area. This, however, predicts turbulence along most of the southern boundary as well as strong turbulence in the western boundary current, where the observed turbulence is mainly present in a small area from $14^\circ E$ to $23^\circ E$. The coarse-resolution completely fails to predict the subpolar turbulent areas.

A section from $0^\circ E$ to $6^\circ E$ and $31^\circ N$ to $37^\circ N$ of the subtropical gyre has been investigated in particular detail. This section includes the western boundary turbulence. In this section, the meridionally averaged values of the depth-integrated turbulent term $(\overline{u'v'})_S$, and the meridional average of depth-integrated velocity shear $(dU/dy + dV/dy)_S$ for both the high-resolution and the coarse-resolution models have been computed. These results are shown in figure 8D. This plot shows

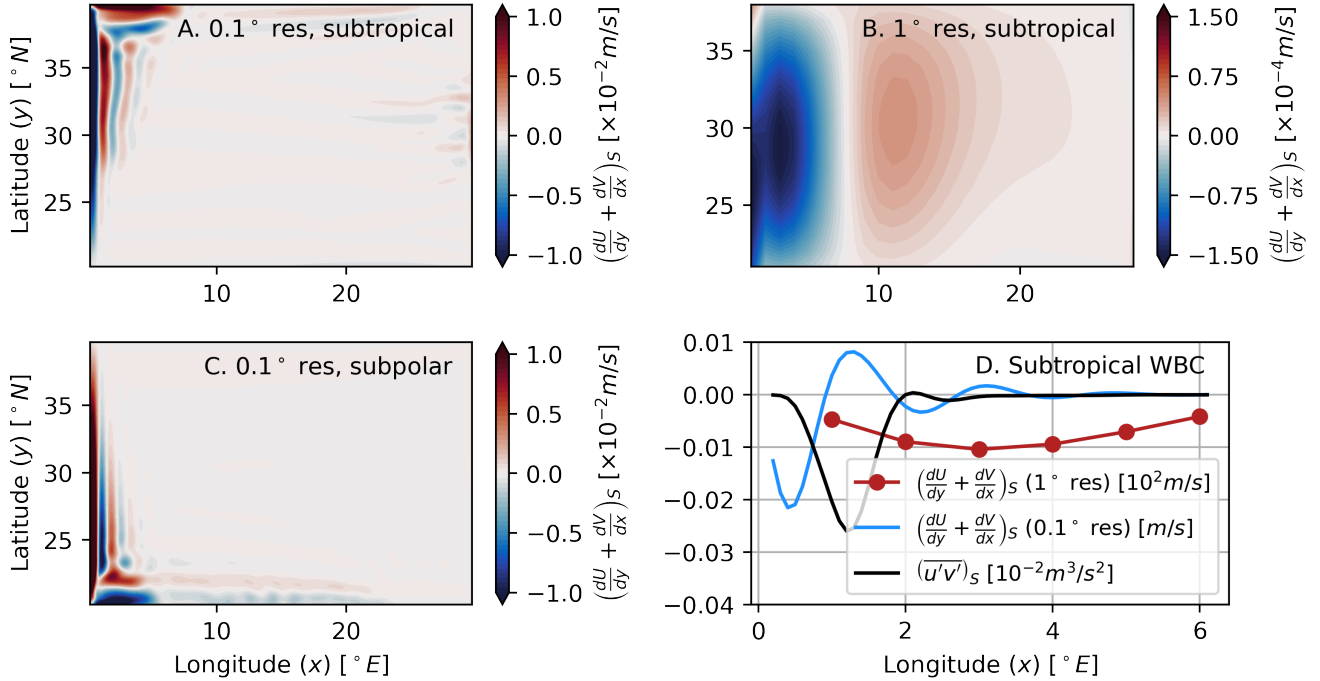


Figure 8: A, B, and C) Velocity shear $dU/dy + dV/dx$ as a function of coordinate for both high-resolution models and for the coarse, subtropical model. D) Meridional averages of the velocity shear for the coarse- and high-resolution subtropical models and of the depth-integrated unsteady term, evaluated in the turbulent western boundary region from $31^\circ N$ to $37^\circ N$ as functions of longitude.

that the high-resolution model shear predicts correctly predicts positive shear in the area where the turbulence is non-zero and negative. However, the shear predicts that most turbulence is present at the boundary, where the observed turbulence is mainly present a small distance $\sim 0.4^\circ E$ away from the boundary. The coarse-resolution model predicts that the turbulence covers a larger zonal extent than what is observed. This is most likely do to the over-estimated western boundary current width of the coarse-resolution model. However, the coarse-resolution model correctly predicts that the turbulence is not significant at the boundary itself.

The present analysis thus shows that for both the high-resolution and the coarse-resolution models, Prandtl’s mixing length model does not consistently predict the presence of turbulence in the areas where turbulence has been observed in the high-resolution model. For the high-resolution models, the mixing length model generally overestimates the extent of turbulence, where for the coarse-resolution models, the extent of turbulence is not consistently under- or overestimated.

4 Discussion

In the present work, a validation element for the four numerical models is to check if they have converged to a steady state. The validation results in figure 1B show that for all four numerical models, the sea surface temperature has not stabilized at a constant level by the end of the spin-up period. While no parts of the present analysis concern temperature or heat, water has a volumetric thermal expansion coefficient on the order of $\alpha_V = 10^{-40} C^{-1}$ at around $10^\circ C$. The average of

the model atmospheric temperature (equation 16) is $7.5^{\circ}C$. At the end of the spin-up period, the average sea surface temperature for all models is around $11.5^{\circ}C$. Assuming that the average sea surface temperature converges to the average atmospheric temperature, the steady state temperature is roughly $\Delta T = 4^{\circ}C$ different from the actual temperature at the time of data collection. This corresponds to a relative density difference on the order of $\alpha_V \Delta T \sim 4 \times 10^{-4}$. This very slight density difference is not expected to have impacted the flow phenomena significantly. Figure 1A shows that while the western boundary current has fully converged for the low-resolution setups, this is not the case for the high-resolution setups. However, figures 2A-B and 3A-D show that the models all satisfy Sverdrup’s balance in the interior, non-turbulent areas. Since the Western boundary current balances the mean flow governed by Sverdrup’s balance, the boundary current strength must reflect a physically plausible steady condition. This indicates that the strength in figure 1A is levelling off. On the basis of this spin-up analysis, the modeled flow is considered representative for realistic, physical flow for the purpose of this present project. For a future development of this project, it is suggested that a longer spin-up period is investigated in order to firmly conclude if the western boundary current is in fact levelling off.

The average streamfunctions (figures 4A-D) show that the subpolar gyre is practically identical but anti-parallel to the subtropical gyre in the coarse-resolution models. This is also reflected in figures 3A-B showing that the structure of the deviation from the predicted meridional transport is very similar for the two setups. The high-resolution setups reveal that the smaller-scale mean flow differs in the two physical situations. This is embodied in the temporally stable, stationary turbulence that is best pictured in figures 3. This figure shows that the meridional transport velocity in the interior of the basin is inhomogenous for the subtropical gyre, while it is relatively constant for the subpolar gyre.

Both the high- and coarse-resolution models picture the western boundary current. While the coarse resolution model predicts a single current and recirculation, the high-resolution models predict several nodes of currents and recirculations. Also, the recirculation extends as far as $\sim 12^{\circ}E$ into the basin (see figure 3) for the coarse resolution model - always halfway into the domain. At its widest point, the western boundary current including all nodes of currents and recirculations extends only $\sim 5^{\circ}$ into the basin for the high-resolution models. For the average heat transport, which is usually an important parameter for ocean models used in climate simulations, overestimating the width of the boundary current may be problematic since a narrower, faster current transports heat at a greater speed than a wide, slow one. This means that a larger heat fraction from the southern latitudes is deposited along the trajectory of the western boundary current than at its endpoint for a coarse-resolution model, which leads to an error in the meridional heat distribution. Thus, there are quantitative mean-flow differences in the overall flow between the high- and coarse-resolution models that may have significance when used in larger climate models.

A difference between the subtropical gyre and the subpolar gyre is that the turbulence is much more dominant and powerful for the subtropical gyre (see figures 5A-D). The main qualitative difference between these two physical systems is that the Ekman pumping is negative (downwelling) in the interior of subtropical gyres and positive (upwelling) in the interior of subpolar gyres [8, Chap. 2]. The turbulent speed is generally lowest near the bottom of the basin (see section 3.4 and appendix A.1). Thus, if a general upwelling is present, low turbulent speed is advected to the center of the basin for the subpolar gyre. For the subtropical gyre, a general downwelling advects the high turbulent

speed near the surface into the center of the basin. This might explain why the subtropical gyre is generally more turbulent than the subpolar gyre and indicates that turbulence is generated mainly at the sea surface. Note that the subpolar gyre model does not represent a realistic system on Earth since the wind fields that cause a subpolar gyre are generally found at higher latitudes than what is used as the present model domain [8, Chap. 2]. Consequently, no experimental evidence exists to confirm this inherent turbulent difference between the two systems. Although not directly applicable Earth’s oceans, this gives insight into general behaviour of turbulent liquids.

In order to test Prandtl’s mixing length model as stated in equation 7 for the high-resolution setups, a search has been conducted for a characteristic length- and velocity scale. Fourier transforms of the instantaneous turbulent transport speed has shown that a characteristic wavenumber is indeed present in the high-resolution models, which corresponds to a characteristic length scale. The analysis failed to find a uniquely defined turbulent velocity scale but rather provided estimates at the upper boundary of the characteristic velocity scale for different turbulent areas.

It is noted that the characteristic length scale appears to be shorter near the western boundary in figure 6C than in the rest of the basin. According to the law of the wall [4], the turbulent speed decreases near a boundary. Since the length scale also decreases, this might indicate that the ratio of the length scale to the velocity is constant, which indicates the existence of a characteristic time scale $t_T = l_T/u_T$. Finding evidence of such a characteristic turbulent time scale is beyond the scope of the present work, but is left as an interesting task for future research.

Testing Prandtl’s mixing length model directly by plotting the unsteady term of the Reynolds-averaged Navier Stokes equations, $\overline{u'v'}$, against the velocity shear, $dU/dx + dV/dy$, did not show the presence of linear correlation as assumed by the mixing length model. This indicates that the effects of turbulence on the mean flow is qualitatively different from that of molecular viscosity, and the present data thus suggests that care should be taken when using the mixing length model for parameterizing sub-grid scale turbulence in numerical ocean models.

In a study by Lévy et al (2018) [6], it was found that increasing the horizontal resolution from 1° to $1/9^\circ$ produced qualitatively different results, which is in accordance with the findings of the present thesis. The study also found that increasing the resolution even further (first to $1/27^\circ$ and then to $1/54^\circ$) produced yet different general characteristics. This indicates that the sub-grid scale turbulence significantly influences the mean flow in a manner not accounted for by the turbulent viscosity. This may be explained by the results of the present report that the mixing length model is in fact not applicable to numerical ocean models.

It thus appears that the only way to build a numerical model that produces results that reflect all turbulent length scales is to resolve all length scales. With length scales of down to $20m$ influencing the mean flow via Stokes drift [3], this is technologically impossible due to computing power limitations. Therefore, Prandtl’s mixing length model may be the only option to estimate effects of inevitable sub-grid scale turbulence. However, according to the present data, the parameterized sub-grid scale flow will remain inappropriately estimated.

5 Conclusion

In the present study, four numerical ocean models have been made and implemented into the Versatile Ocean Simulator (VEROS), representing a subtropical gyre and a subpolar gyre. Both gyres have

been modeled using a high horizontal resolution of 0.1° and a coarse horizontal resolution of 1° . A model validation analysis showed that while the models have not converged completely, they do represent physically plausible scenarios.

The results show that the coarse-resolution models predict a western boundary current that is much wider and more uniform than that predicted by the high-resolution models. Since the western boundary current is responsible for much of Earth’s meridional heat transport, over-estimating its width by using a coarse resolution may lead to poor whole Earth model simulations.

Prandtl’s mixing length model parameterizes the unsteady term of the Reynolds averaged Navier-Stokes equations via the mean velocity shear based on a characteristic turbulent length- and velocity-scale. This study finds that a characteristic turbulent length scale of $(150 \pm 30)km$ is indeed present in the high-resolution models. A unique, characteristic turbulent velocity has not been found, however. Also, this study finds that Prandtl’s mixing length model fails to parameterize the structure of the observed turbulence in the high-resolution models based on the mean flow of both the high- and low-resolution models.

The linear correlation between the mean velocity shear and the unsteady term of the Reynolds averaged Navier-Stokes equations predicted in the mixing length model has not been found in any of the turbulent regions in the high-resolution models. This means that, according to the present data, one has to be critical to results obtained using Prandtl’s mixing length model - at least in the presently investigated regimes. Thus, in principle, the only way to produce reliable ocean models is to resolve all relevant length scales.

References

- [1] James W. Hurrell et al. “The Community Earth System Model A Framework for Collaborative Research”. In: *Bulletin of the American Meteorological Society* 94.9 (2013), pp. 1339–1360.
- [2] R. J. Barlow. “Statistics”. In: 1st ed. John Wiley and Sons, 1989.
- [3] T. S. van den Bremer and Ø. Breivik. “Stokes Drift”. In: *Philosophical Transactions A* 376.2111 (2017).
- [4] Theodor von Karman. “MECHANICAL SIMILITUDE AND TURBULENCE”. In: *Nachrichten von der Gesellschaft der Wissenschaften zu Gottingen* NACA-TM No. 611 (1931).
- [5] Pijush K. Kundu et al. “Fluid Mechanics”. In: 6th ed. Academic Press, 2016.
- [6] M. Levy et al. “Modifications of gyre circulation by sub-mesoscale physics”. In: *Ocean Modelling* 34.1–2 (2010), pp. 1–15.
- [7] Joseph Pedlosky. “Geophysical Fluid Dynamics”. In: 2nd ed. Springer, 1987. Chap. 5.
- [8] Joseph Pedlosky. “Ocean Circulation Theory”. In: 1st ed. Springer, 1996.
- [9] Conor Purcell. “A sharper view of the world’s oceans”. In: *Nature* 575 (2019), pp. 6–8.
- [10] Detlef Stammer. “Global Characteristics of Ocean Variability Estimated from Regional TOPEX/POSEIDON Altimeter Measurements”. In: *Journal of Physical Oceanography* 27 (1997), pp. 1749–1758.

A Appendix

A.1

Figure 9

A.2

Figure 10

A.3

Figure 11

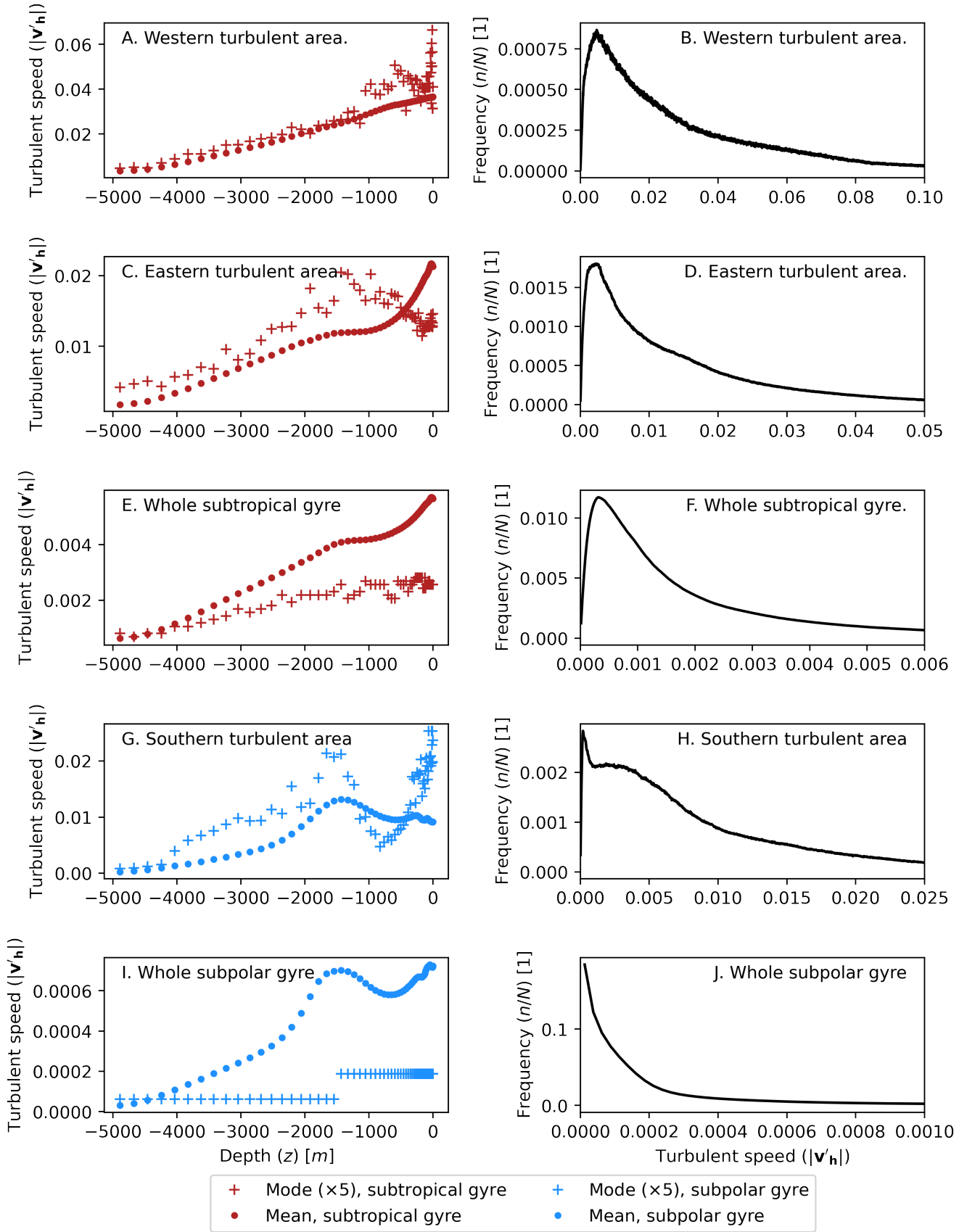


Figure 9: Left panels: modes and means of the turbulent speed distribution as functions of depth in the specified regions. Right panels: Histograms of the turbulent speed distribution based on measurements from all grid points in the specified region.

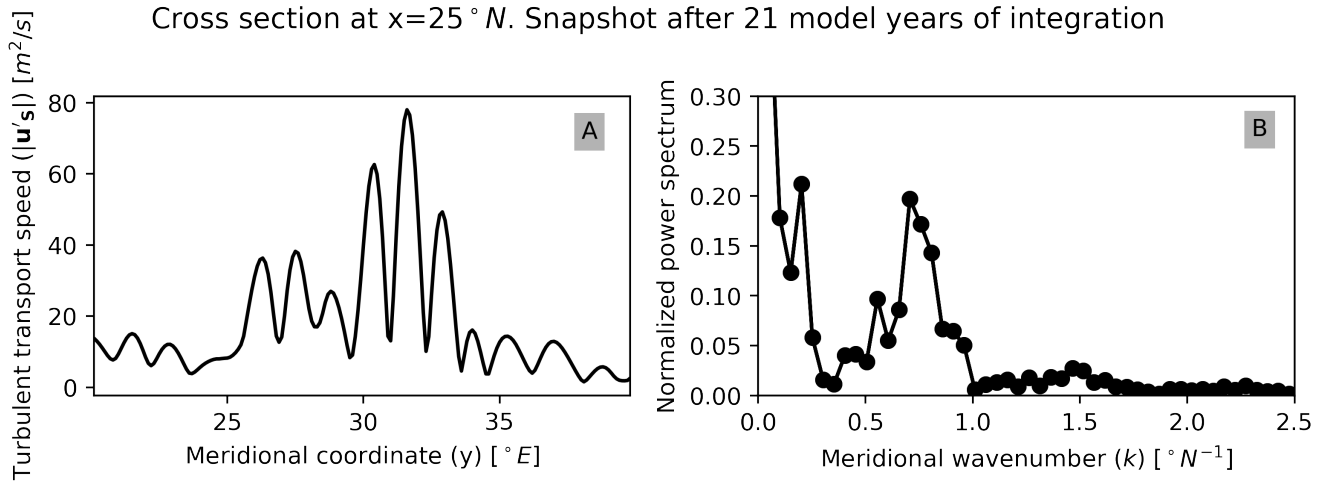


Figure 10: Example of a cross section from the subtropical gyre model of the turbulent transport (A) and the corresponding normalized power spectrum of wavenumbers (B).

	High-resolution models	Low-resolution models
Horizontal resolution	0.1°	1°
Timestep	150s	900s
Lateral biharmonic viscosity	$10^{11}m^4/s$	None
Lateral biharmonic diffusivity	$10^9m^4/s$	None
Isopycnal diffusivity	$10m^2/s$	$1000m^2/s$
Isopycnal diffusivity (steep slopes)	$200m^2/s$	$500m^2/s$
Skew diffusion	Enabled	Enabled
Horizontal viscosity	None	$2.199 \times 10^5m^2/s$
Bottom friction coefficient	$10^{-5}s^{-1}$	$10^{-5}s^{-1}$
Implicit vertical friction	Enabled	Enabled
TKE	Enabled	Enabled
Thickness diffusion	10	1000
Equations of state type	Nonlinear with compressibility	Nonlinear with compressibility

Figure 11: The settings used for the high- and coarse-resolution numerical models